Charge transport in silicon nanocrystal superlattices in the terahertz regime

H. Němec,[1] V. Zajac,[1,2] P. Kužel,[1,*] P. Malý,[2] S. Gutsch,[3] D. Hiller,[3,†] and M. Zacharias[3]

[1]*Institute of Physics ASCR, Na Slovance 2, 18221 Prague 8, Czech Republic*

[2]*Faculty of Mathematics and Physics, Charles University in Prague, Ke Karlovu 3, 12116 Prague 2, Czech Republic*

[3]*IMTEK Faculty of Engineering, Albert-Ludwigs-University of Freiburg, Georges-Köhler-Allee 103, 79110 Freiburg, Germany*

(Received 23 December 2014; revised manuscript received 15 April 2015; published 28 May 2015)

Silicon nanocrystals prepared by thermal decomposition of silicon-rich 2–5-nm-thick SiO_x layers ($0.64 \leqslant x \leqslant 1$) are investigated using time-resolved terahertz spectroscopy. The samples consist of a superlattice of isolated monolayers composed of Si nanocrystals with controlled variable size and filling fraction. Experiments with variable optical pump fluence over almost two orders of magnitude allow us to determine the depolarization fields in the structure. Careful consideration of the local fields along with Monte Carlo calculations of the microscopic conductivity of Si nanocrystals supported by structural characterization of the samples provide detailed information about the electrical connectivity of nanocrystals and about the charge transport among them. Well below the percolation threshold, nanocrystals grow mostly isolated from each other. In thicker or in more Si-enriched layers, nanocrystals merge during their growth and form tens-of-nanometer-sized photoconducting Si structures with a good electrical connection. In addition, in thick SiO_x layers, imperfectly connected clusters of Si nanocrystals are observed which develop probably at the end of the growth process and allow only limited charge transport due to energy barriers.

DOI: 10.1103/PhysRevB.91.195443 PACS number(s): 78.47.J−, 73.63.Bd

I. INTRODUCTION

Silicon is the most important material for current electronics. In its bulk form, it is an indirect semiconductor with very long radiative lifetimes of free carriers. Nonradiative recombination at material imperfections thus dominates, which prevents operation of Si-based light-emitting devices. Quantum confinement leads to significantly enhanced radiative recombination and a band-gap shift towards the visible region, which is of fundamental importance for many prospective applications, including photovoltaic devices [1], fluorescence labeling of living cells, cancer tumors, and targeted drug delivery [1,2], light sources and waveguides for silicon photonics [1–3], and Si nanocrystal-based memories [1–3].

Charge transport in individual quantum dots has been investigated thoroughly in the past [4]; however, a deeper knowledge is still lacking about charge transport among nanometer-sized nanocrystals (NCs) in larger ensembles. Although it is possible to attach electrodes to a single nano-object [5], an application of such methods is not convenient on large ensembles of nanoparticles since they do not permit one to easily distinguish, e.g., between the inter- and intrananoparticle charge transport. In this situation, it is advantageous to probe the microscopic mobility as a nanoscale response function of charge carriers within the larger ensembles in a noncontact way. In this paper, we apply time-resolved terahertz (THz) spectroscopy [6] to the investigation of Si NCs fabricated by thermal decomposition of silicon-rich SiO_x layers ($0.64 \leqslant x \leqslant 1$) in SiO_2/SiO_x multilayers. The high frequency of the probing radiation allows sensing of the charge motion directly on nanometer scales [7]. Proper analysis of THz conductivity spectra then allows retrieval of information on both intra-NC charge transport [8] and charge transport within aggregates of NCs [9]. The charge transport can be deeply influenced by depolarization fields; in larger nano-objects, this contribution usually determines the characteristic shape of THz spectra with increasing real part and negative imaginary part of the transient conductivity [10]. Such behavior was reported, e.g., in works investigating the charge transport along the large dimension of various nanowires in nonpercolated ensembles [11–13]. In systems containing small nonpercolated nanoparticles, the localization of charges due to their interaction with the nanoparticle boundaries and the depolarization fields may play an equal role. In such a case, control of the strength of depolarization fields through a scaling of the photoconductivity by the excitation fluence allows one to disentangle these two phenomena and makes it possible to assess the morphology, namely, the degree of percolation of the photoconducting component [14,15].

Time-resolved THz spectroscopy was recently used for an investigation of Si NCs prepared by thermal decomposition in a 1-μm-thick $SiO_{x=1}$ layer with variable annealing temperatures [7,16]. These experiments were interpreted within the framework of the phenomenological Drude-Smith model [17], suggesting a picture of a localized behavior of carriers with the possibility of their transfer among nanocrystals and redistribution to larger nanocrystals at later times after optical injection. The photoconductivity decay observed on ∼100 ps time scale was attributed to the carrier trapping at unpassivated surface states of nanocrystals. Later works studied samples with various compositions controlled by the Si content of 0.2- or 1-μm-thick silicon-rich SiO_x layers, $x = 0.2-1.4$ in [18] and $x = 0.2-1.0$ in [19], which allows tuning the Si NC volume fraction from 80% down below the percolation threshold close to 35%. The change in the transport nature was clearly detected near the percolation threshold. In percolated samples, the Drude-Smith fits indicate a transition from initial long-range internanocrystal transport to more localized states on a tens-of-picoseconds time scale.

*kuzelp@fzu.cz

†daniel.hiller@imtek.uni-freiburg.de

 ©2015 American Physical Society

Depolarization fields are inevitably induced in inhomogeneous materials [20,13]. Moreover, all of the above-mentioned experiments on Si NCs [7,16,18,19] were carried out at relatively high pump fluences ($0.3-1.4$ mJ/cm^2) leading to carrier densities markedly exceeding 10^{18} cm^{-3}. At these photocarrier densities, the depolarization fields usually play an important role [21]. However, experiments with systematic variation of the pump fluence have not been performed and the depolarization fields were not considered in this class of samples so far. In our understanding of the underlying phenomena, fitting with the Drude-Smith model in such a case leads to an encoding of the influence of the depolarization fields into the Drude-Smith's parameters in a nontransparent way and their interpretation is not straightforward. Particular attention should be devoted to the analysis of THz spectra of sub-10-nm-sized nanocrystals, as there is a high risk that the response is fundamentally affected by larger particles from the tails of the size distribution [15].

The samples studied in the present paper possess a variable composition and layer thickness: it is possible to independently control the NC size and concentration. Moreover, nanometer-thick SiO_x layers are sandwiched between isolating barriers, which ensures that the arrangement of the NCs is only two dimensional, without possibly very complex percolation properties in the third dimension (out-of-plane direction). Experimentally, we acquire data over two orders of magnitude of the pump fluence, which allows us to consider in detail the role of depolarization fields. We employ microscopic (nonphenomenological) models of the THz conductivity in semiconductor NCs, which directly reflect their microscopic properties. These considerations make it possible to determine the morphology of the nanocrystalline structure, to estimate the coupling between NCs, and to assess the efficiency of charge transport in such structures.

II. EXPERIMENT

The Si NCs were prepared by the superlattice approach described in detail in [22]. In brief, silicon-rich amorphous oxides SiO_x were sandwiched between diffusion barriers for silicon (here, SiO_2). Subsequently, high-temperature treatment (1150°C, 1 h, pure N_2 atmosphere) induced phase separation of the silicon-rich oxide and crystallization of the resulting Si clusters. In this way, the size of the Si NCs is tuned by the SiO_x layer thickness, whereas the in-plane density of Si NCs is adjusted by the amount of Si excess within the silicon-rich layer. In order to reduce the density of dangling bond defects at the $Si-NC/SiO_2$ interface, all samples were postannealed in pure H_2 ambient (500°C, 1 h) [23].

The superlattice structure was prepared by plasma-enhanced chemical vapor deposition (PECVD) in a Plasmalab 100 reactor (Oxford Instruments) with a 13.56 MHz driven parallel plate reactor [24]. A N_2O/SiH_4-based precursor chemistry allows achieving various silicon oxide compositions as a function of their gas flow ratio. As a consequence, a significant amount of nitrogen (∼10 at%) is incorporated in the silicon-rich films. The precursor gases were diluted by a high flow of Ar in order to increase the film homogeneity and decrease the growth rate. The films were grown at a temperature of 375°C, a chamber pressure of 600 mTorr, and a plasma source power of 13 W, resulting in the growth rates of about 2 Å/s.

The properties of prepared samples are summarized in Table I. They can be divided into two series. In the first series (M100, M93, M85, M64), the thickness of SiO_x layers is kept constant at 3.5 nm while the concentration of oxygen in these layers is systematically changed (from $x = 1$ down to 0.64). In contrast, in the second series (S93, M93, L93), the thickness of Si-rich layers is varied (2.0 nm = Small, 3.5 nm = Medium, and 5.0 nm = Large, respectively) and the concentration of oxygen is constant ($x = 0.93$).

The transient THz conductivity spectra were measured in a usual setup for time-resolved THz spectroscopy [25] driven by a Ti:sapphire laser amplifier (Spitfire ACE, central wavelength 800 nm, 1 mJ pulse energy, 5 kHz repetition rate). A part of the laser beam was used as an optical pump; for this purpose, it was frequency doubled to 400 nm (3.10 eV) and defocused to generate photocarriers homogeneously across the sample. The other part of the output laser beam was used for the THz pulse generation and its phase-sensitive detection using the optical rectification and electro-optic sampling, respectively. The experiments were carefully performed as a function of the photocarrier density: the intensity of the pump beam was gradually decreased by neutral density filters.

We wish to stress that we focus on in-plane transport which we easily access owing to the transverse polarization of the THz radiation. Vertical charge transport was studied using conventional techniques, e.g., in [26,27].

TABLE I. Summary of properties of the investigated samples.

	Nominal properties		Optical properties		TEM				THz data					
Sample	SiO_x thickness (nm)	x	Transmission (%)	α_{eff} (cm^{-1})	s_{area} (%)	s_{vol} (%)	$\langle d\rangle$ (nm)	$\langle d\rangle_{d^2}$ (nm)	V_d	$p_{F,d}$ (%)	δ (nm)	s_δ/s_{vol} (%)	V_δ	$p_{F,\delta}$ (%)
M100	3.5	1.00	79	11000	Data not available				0	0	–	–	–	–
M93	3.5	0.93	70	19000	17.7	11.8	2.6	3.0	0	0	–	–	–	–
M85	3.5	0.85	73	16000	22.3	14.9	3.0	3.6	0	0	–	–	–	–
M64	3.5	0.64	52	41000	24.6	16.4	3.2	4.4	0	0	29	5	0.0012	0
S93	2.0	0.93	83	12000	Data not available				0	0	–	–	–	–
M93	3.5	0.93	70	19000	17.7	11.8	2.6	3.0	0	0	–	–	–	–
L93	5.0	0.93	41	41000	30	20	3.4	4.7	0	4	16	30	0.0015	0

III. TERAHERTZ SPECTRAL RESPONSE

A. Effective conductivity

Free carriers in bulk semiconductors are usually described by a simple Drude model or by one of its modifications reflecting the relaxation-time distribution [28]. Nanoscaled materials are inherently inhomogeneous and their macroscopic response (THz photoconductivity) usually significantly differs from this case. Two major reasons for this behavior should be pointed out:

(1) Charge confinement in the NCs (either a quantum confinement or an interaction of classically described charge carriers with NC boundaries). These interactions control the dynamical mobility of charges μ and their microscopic conductivity $\Delta\sigma_\mu = eN\mu$, where e is the elementary charge and N is the photocarrier density. Note that we understand the dynamical mobility $\mu(\omega)$ as a spectral response function of a single carrier to the *local* electric field and we call it *microscopic mobility* throughout this paper (not to be confused with the dc or drift mobility, which is a single value describing a long-range transport). We calculate the mobility using the Monte Carlo method described in Sec. III C.

(2) The macroscopic photoconductivity $\Delta\sigma_{\text{eff}}$ (which is actually measured) reflects an effective response of charge carriers to an *external* (probing) THz electric field. The relation between the macroscopic and microscopic photoconductivities is usually nonlinear and can be described by a suitable effective medium theory [14,21].

In [14], we have shown that the relation between the effective and microscopic conductivities can be, in most systems, described using the "*VBD*" formula,

$$\Delta\sigma_{\text{eff}} = V\Delta\sigma_\mu + \frac{B\Delta\sigma_\mu}{1 + iD\Delta\sigma_\mu/(\omega\varepsilon_0)}, \tag{1}$$

where ε_0 is the vacuum permittivity, V and B represent the weights of the percolated and nonpercolated components, respectively, and D is related mainly to the shape of inclusions in the nonpercolated part. These coefficients are defined by the sample morphology and they do not depend on frequency and photoexcitation density. For low microscopic conductivities, achieved upon weak photoexcitation, the depolarization fields are weak and $\Delta\sigma_{\text{eff}}$ is directly proportional to $\Delta\sigma_\mu$:

$$\Delta\sigma_{\text{eff}}(\omega) \approx (V + B)\Delta\sigma_\mu(\omega). \tag{2}$$

Upon increasing the excitation intensity, the second right-hand term in (1) enters into a nonlinear regime and eventually it saturates for very high carrier concentrations. The determination of the dependence of $\Delta\sigma_{\text{eff}}$ on the excitation fluence is thus an essential experimental step for an assessment of the degree of percolation in the sample.

Note that Eq. (1) reduces to the Maxwell-Garnett effective medium approximation for specific values of the coefficients [15]:

$$\begin{aligned} V &= 0, \\ B &= \frac{\varepsilon_{\text{SiO2}}(1 + sK) - \varepsilon_{\text{eff}}(1 - s)}{\varepsilon_{\text{SiO2}}(s + K) + \varepsilon_{\text{Si}}(1 - s)}, \\ D &= \frac{(1 - s)}{\varepsilon_{\text{SiO2}}(s + K) + \varepsilon_{\text{Si}}(1 - s)}, \end{aligned} \tag{3}$$

where $\varepsilon_{\text{SiO2}} \approx 4$ and $\varepsilon_{\text{Si}} \approx 12$ are the THz permittivities of the SiO_2 matrix and Si NCs, respectively, s is the filling fraction of Si inclusions, the shape factor K equals 2 for spherical inclusions, and the effective equilibrium permittivity ε_{eff} is calculated e.g., using Eq. (11) in [29].

The Maxwell-Garnett model is strictly valid only when the silicon NCs do not form any percolation path ($V = 0$). However, in order to allow for a quantitative analysis close to the percolation threshold, we will assume that the same relation between the coefficients B, D and the filling factor s holds also for percolated samples with very small percolation strength, i.e., when V acquires small nonzero values. Under this assumption, we eliminate the need to consider the values of B and D as unknown (fitting) parameters; instead, they will be directly related to the sample stoichiometry through the filling fraction s, and V remains the only unknown morphology parameter.

B. Transient terahertz transmission

The propagation of THz pulses in inhomogeneous media was studied in detail in [15] and [21]. The key measurable quantity in thin-film samples is the normalized transient transmission ΔT_{norm} which is proportional to the transient THz transmission spectra $\Delta E_t/E_t$,

$$\Delta T_{\text{norm}}(\omega) = -\frac{1 + n_{\text{SiO}_2}}{z_0}\frac{1}{e\phi}\frac{\Delta E_t(\omega)}{E_t(\omega)}, \tag{4}$$

where ϕ is the optical pump photon fluence (in photons/cm^2 per pulse), n_{SiO2} is the refractive index of the SiO_2 substrate, z_0 is the vacuum wave impedance, and e is the elementary charge. This quantity has the dimension of the mobility ($\text{cm}^2\text{V}^{-1}\text{s}^{-1}$) and it has been shown to be equal to a transient sheet conductivity normalized by the charge and pump photon fluence,

$$\Delta T_{\text{norm}} = \frac{\int_0^L \Delta\sigma_{\text{eff}}(\omega, z)dz}{e\phi}. \tag{5}$$

Note that the z dependence of the photoconductivity $\Delta\sigma_{\text{eff}}$ stems from the inhomogeneous distribution of the charge-carrier concentration $N(z)$. For homogeneous materials, this dependence is exponential (following the Lambert-Beer absorption law) and one easily finds $\Delta T_{\text{norm}} = \xi \cdot \mu(\omega)$ (where ξ is the quantum yield of the charge-carrier generation) [14]. This simply relates the measured transient transmission with the microscopic carrier response $\mu(\omega)$ which is to be determined.

In contrast, the dependence $\Delta\sigma_{\text{eff}}(z)$ may become quite complex in inhomogeneous samples due to the nonlinear character of the conductivity contribution of nonpercolated parts described by the second right-hand term in (1). It was shown that for a thin film with thickness L [21],

$$\begin{aligned} \Delta T_{\text{norm}} = {} & V\Delta\sigma_\mu^{\text{norm}} \\ & + B\frac{\text{Ln}[1 + Y_0] - \text{Ln}[1 + Y_0\exp(-\alpha_{\text{eff}}L)]}{Y_0}\Delta\sigma_\mu^{\text{norm}}, \end{aligned} \tag{6}$$

where $\Delta\sigma_\mu^{\text{norm}}$ is the normalized transient conductivity (per single unit charge) at the input surface of the photoexcited

sample,

$$\Delta\sigma_{\mu}^{\mathrm{norm}}(\omega) = \frac{\Delta\sigma_{\mu}(\omega, z=0)}{e\alpha_{\mathrm{eff}}\phi} \equiv \frac{\alpha_{\mathrm{Si}}}{\alpha_{\mathrm{eff}}}\,\xi\,\mu(\omega) \tag{7}$$

and

$$Y_0(\omega) = i\,\frac{D}{\varepsilon_0\omega}\,e\phi\alpha_{\mathrm{Si}}\,\xi\,\mu(\omega). \tag{8}$$

The optical absorption is characterized by two important parameters: (i) The absorption coefficient of silicon α_{Si} determines the photocarrier concentration *inside* the NCs for a given photon fluence, i.e., it is an intrinsic property of NCs independent of their surroundings. (ii) The effective absorption coefficient α_{eff} describes the attenuation of the pump fluence with depth in the composite sample, i.e., it takes into account the dilution of NCs in the transparent SiO_2 matrix and the morphology of NCs network [21].

The formula (6) constitutes the basic relation between the measured transient transmission and the microscopic response represented by the mobility spectrum $\mu(\omega)$. In our case, we consider L as the cumulative thickness of all SiO_x layers in the sample. For the lowest excitation levels and for an entirely percolated sample, the nonlinear character of (1) and (6) disappears and the measured ΔT_{norm} (i.e., normalized transient sheet conductivity) directly corresponds to the microscopic response of the NCs $\Delta\sigma_{\mu}^{\mathrm{norm}}$. If, on the other hand, ΔT_{norm} scales with the pump photon fluence ϕ, the depolarization fields develop in the nonpercolated parts of the sample and their effect is encoded into the second right-hand term of (6). The measurements of differential transmission spectra versus charge-carrier concentration (pump fluence) are thus vital for assessing the sample morphology and percolation strength.

C. Microscopic mobility

Mobility spectra of Si NCs were calculated using the Monte Carlo approach described in detail in [30]. In brief, the thermal motion of charges was simulated in quasiclassical approximation and their mobility was subsequently determined from the velocity autocorrelation function using the Kubo formula. By using this approach, we can account for the intrananocrystal charge-carrier motion, which is limited by the NC diameter d, as well as for the internanocrystal charge transport described in terms of the probability p_{F} of the carrier transmission through a NC boundary into an adjacent NC [30]. In bulk silicon, τ_{s} is typically longer than 100 fs, which results in mean free paths much longer than the dimensions of NCs. In turn, the scattering rate in bulk is negligible compared to the frequency of interactions with the surface; therefore the mobility spectra are completely determined only by the parameters d and p_{F}.

We wish to stress that charges in the Si NCs under study are subject to a strong confinement where, strictly speaking, exciton levels should be considered instead of the bandlike charge transport [31]. Density-functional-theory calculations [32] show that the spacing of electron states in isolated NCs with a 2.5 nm diameter does not exceed 0.2 eV. On the one hand, such energy spacing is considerably larger than the thermal energy at 300 K. On the other hand, the energy-level separation pertinent for our experiments will be lower, namely due to the larger mean diameter of NCs contributing to the THz signal, but also due to the embedding of NCs into the glass matrix which will lead to coupling between the NCs and matrix states. In this situation, we believe that the employed semiclassical calculations still capture the principal aspects of the carrier response at room temperature, even for the smallest investigated NCs.

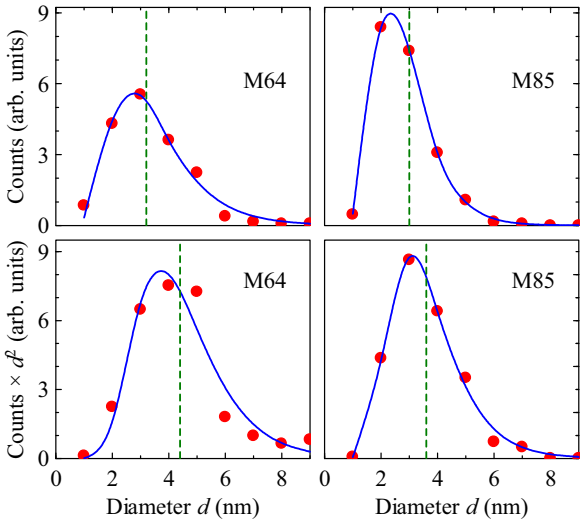

FIG. 1. (Color online) Examples of distributions of NC sizes. Symbols: distribution determined from EF-TEM images; solid lines: fit using log-normal probability distribution; vertical dashed lines: mean values. Upper panels display a direct number-of-particle distribution; lower panels show the number-of-particle distribution weighted by d^2.

IV. SAMPLE MORPHOLOGY AND OPTICAL PROPERTIES

The structure of the samples observed by energy-filtered transmission electron microscopy (EF-TEM) [33] was used to determine the areal filling fraction s_{area} and the mean size of Si NCs (Fig. 1; examples of EF-TEM images are shown in [34]). The optical and THz response of the layers is controlled by the volume filling fraction s rather than by the areal one, therefore we will assume that the NCs are spherical, in which case $s = 2s_{\mathrm{area}}/3$.

The absorption of optical pump pulses defines the concentration of conduction-band carriers in the NCs and, as explained in Sec. II, this concentration is a crucial parameter in the evaluation of the NC properties. In the analysis of our experimental results, we will assume that the absorption coefficient of Si in NCs, α_{Si}, is the same as that of bulk silicon (7×10^4 cm^{-1}) and that the quantum yield of the mobile carrier generation $\xi \approx 1$. This assumption and the relation between α_{eff}, α_{Si}, and ξ are discussed in detail in the Appendix.

V. FITTING MODEL

The fitting model for the normalized transmission function ΔT_{norm} is constructed as follows:

(1a) The spectra of microscopic mobility $\mu(\omega)$ are calculated using the Monte Carlo method [30]. The input parameters here are the mean diameter d of the NCs (fixed to the value

obtained from EF-TEM; Table I), the probability of inter-NC charge transport p_F, and the bulk electron mean scattering time τ_s. The spectra are calculated at room temperature, $T = 300$ K. The contribution to the conductivity of NCs with a given size d is not proportional to the number of such NCs, but rather to their total volume, which means that the number-of-particle distribution should be appropriately weighted. From the EF-TEM images, we do not have information about the height of the NCs and we assume that the height corresponds to the thickness of the layer. For this reason, we consider the in-plane distribution of NC sizes as decisive for their response and we weigh the number-of-particle distribution by d^2 (bottom plots of Fig. 1). The mean value of d in this weighted distribution was then considered in the calculations.

(1b) It will be shown later that larger NCs or clusters of NCs are formed in some samples. We will approximate the response of these larger particles by the response of larger NCs with diameter δ. Indices d and δ are then used to distinguish between parameters corresponding to individual NCs and to clusters.

(2) The theoretical value of the normalized transient transmission is calculated using Eq. (6). The adjustable parameter here is the percolation strength V. The other parameters are defined by the morphology (B and D through the volume filling fraction s) or by intrinsic properties of the material (α_{Si},α_{eff}). The quantum yield $\xi = 1$, as justified in the Appendix.

(3) The calculated spectra of ΔT_{norm} are fitted to the experimental ones. The fitting parameters are V, p_F, and τ_s. However, the bulk scattering time τ_s is found to be larger than 100 fs in all the spectra and does not influence at all the response of confined carriers for the given NC sizes. In some fits, a second confinement scale must be introduced (existence of clusters); in this case, two additional parameters are used: cluster size δ and cluster filling fraction s_δ.

A common fit with a single set of these fitting parameters is always performed for a complete series of complex-valued spectra belonging to one sample measured at various pump fluences.

VI. RESULTS AND DISCUSSION

Examples of transient transmission spectra measured 10 ps after photoexcitation are shown in Fig. 2. The common feature of all the spectra is a dominating negative imaginary part and the fact that the normalized transmission ΔT_{norm} (or, equivalently, normalized transient sheet conductivity) somewhat decreases with increasing excitation fluence. These features are typical signs of a predominantly capacitive response of the sample due to depolarization fields in nonpercolated structures [29].

Before providing a more detailed description of the spectra, let us briefly discuss the experimental errors of the data. The error bars in Fig. 2 indicate the statistical error: normal deviation calculated over extended accumulations of spectra. In addition, several kinds of systematic errors appear which, in many cases, will dominate over the statistical errors; here we mention the largest ones. (i) The measurements of pump fluence are done with an accuracy of 10–20%; this includes the precision of the head used for the power measurement, effects of spatial variation of the pump beam intensity, and the overlap between the pump and THz beams. The latter two effects are minimized in our case owing to defocusing the pump beam on the sample. Note, however, that in some cases they can slightly change the spectral shape [35]. The long-term drift of the pump and probe beam power reaches a few percent. As we measure the excitation power and the reference THz wave form both before and after the transient measurements, this error in amplitude is smaller than 2%. (ii) The long-term drift in the zero time of the THz wave form does not exceed 20 fs and it is negligible in comparison with other systematic errors.

We fit the dependence of both the real and imaginary part of ΔT_{norm} as a function of frequency and excitation fluence with a single model which depends on global parameters only. Following the above discussion on experimental errors, it is obvious that one can hardly expect the fitting curves to stay within the statistical error bars. To a large extent, we obtain a very good quantitative agreement between the spectra and the fits both in the frequency and in the carrier density dependence; a required scaling of the order of 10% of some of the curves can be attributed to the error in the measurement of the excitation fluence.

Let us first illustrate some fundamental properties using the spectra of sample M64 [Fig. 2(a)]. For this sample, we reach such low excitation intensity that the normalized transmission ΔT_{norm} (which is equal to the normalized sheet conductivity) no longer depends on the excitation fluence [the data for 3.6×10^{13} and 9.0×10^{12}photons/cm^2 can be considered to correspond to approximately the same response while the pump intensity differs by a factor of 4 in Fig. 2(a)]. In this linear regime, the depolarization fields are negligible and the spectra ΔT_{norm} are simply proportional to the microscopic response $\mu(\omega)$. This is described theoretically by (6) and (7) in the low pump fluence limit, i.e., $Y_0 \ll 0$, for which $\Delta T_{norm} = (V + B)\Delta\sigma_\mu^{norm}$. Attaining this regime was possible only for sample M64: although it exhibits one of the largest signals, the measurement of the spectra for the lowest excitation fluence required accumulations of data over 15 hours. Qualitatively, the observed response $\mu(\omega)$ resembles that of confined carriers within nanoscale objects, similar qualitative conclusions are expected also for samples with a smaller concentration of Si.

Quantitatively, the spectra of samples M93 and M85 are best matched by the theoretical model assuming that there is no percolation or connectivity of the NCs, i.e., $V = 0$ and $p_F = 0$, respectively. Note that there is no other available adjustable parameter for these spectra. Despite this fact, we find a very good quantitative agreement between the measured and the calculated real and imaginary part of the conductivity in a series of spectra for several excitation densities and for several samples with different s and d. Although no EF-TEM data are available for the samples S93 and M100, we verified by scanning over an interval of filling factors that the nature of the response of these samples is the same: the THz spectra confirm the lack of percolation and of inter-NC connectivity.

The quantitative analysis of the response of sample M64 is more complex. In particular, the real part of the conductivity increases quite rapidly with frequency in the accessible spectral window, and also the imaginary part is no longer strictly proportional to the frequency. Such a spectrum is incompatible with the response of nanometer-sized NCs, and it can be explained only by the presence of a non-negligible amount

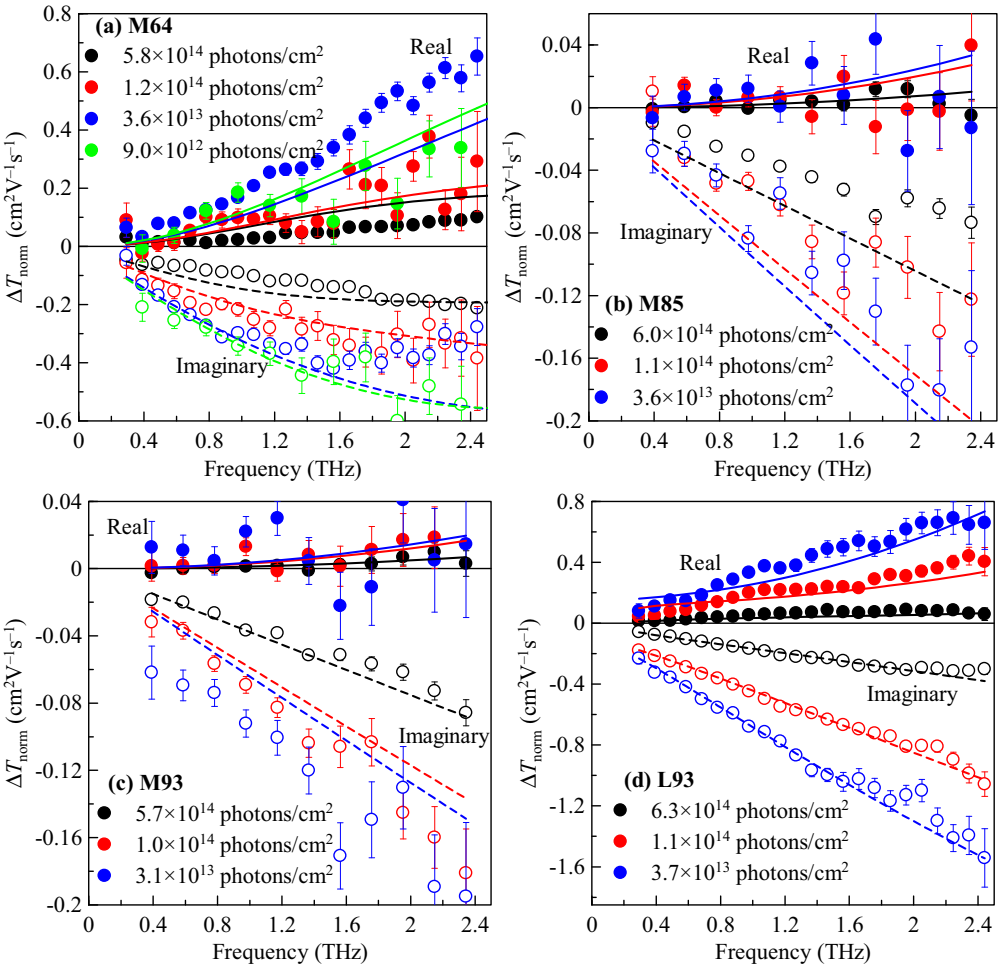

FIG. 2. (Color online) Examples of spectra of the normalized transient transmission ΔT_{norm} [or, following (6), to the normalized sheet conductivity] measured for pump-probe delay of 10 ps (symbols) and fits using the model described in the text (lines). Error bars denote the normal deviation (1σ) calculated over a large statistical ensemble of spectra (50–4000) measured in the time domain with 30 ms time constant. In some cases, these error bars are smaller than the size of symbols. Systematic errors are discussed in the text.

of larger (tens-of-nm) sized particles (cf. the dependence of mobility spectrum on the NC size illustrated in Fig. 3). This suggests that small NCs in this sample merge with each other to some extent, thus forming larger clusters (Fig. 4). In reality, a broad distribution of shapes and sizes is expected to exist with a significant tail towards larger dimensions, similarly as illustrated in [15]. To enable quantitative estimates, we considered in the fitting procedure the existence of NCs with two different sizes: one corresponding to the mean diameter determined from EF-TEM images (d) and the other (adjustable) corresponding to the mean size of the clusters (δ).

The best match is then obtained for a cluster size of 29 nm and $s_\delta/s = 5\%$ (volumic fraction of clusters among all NCs). All parameters are summarized in Table I. A percolation onset is observed: the fitted percolation strength of the clusters is still rather small ($V_\delta = 0.0012$), but a nonzero value is required for reproducing the fluence independence of ΔT_{norm} at the smallest excitation densities when the response of the larger objects dominates. The motion of charge carriers inside the clusters is not hindered by any barriers or geometrical bottlenecks, which means that the connections between the NCs forming the clusters do not contain defects reducing the conductivity. We think this means that in these Si-rich layers, the clusters are formed in the early stages of phase separation during annealing.

Note that as already pointed out in [21], the nonvanishing percolation strength obtained from THz data does not strictly mean a continuous photoconducting pathway through the entire sample, but only on a distance substantially longer than the size of the insulating gaps between the photoconductors (equivalently, this means morphologies with a large depolarization factor). Indeed, each nanostructure can be described by an equivalent electrical circuit [14] where the resistance corresponds to the photoconducting component and the capacitance is determined by the gap between the photoconductors. Morphologies with very small gaps between NCs imply a high capacitance between the photoconductive elements, and upon aggregation into clusters, some of the gaps close, i.e., the capacitance effectively increases whereas the resistance remains unchanged [Fig. 4(b)]. Due to the high probing frequency, the impedance of the capacitor is small and the circuit impedance is dominated by the resistance mimicking the percolation.

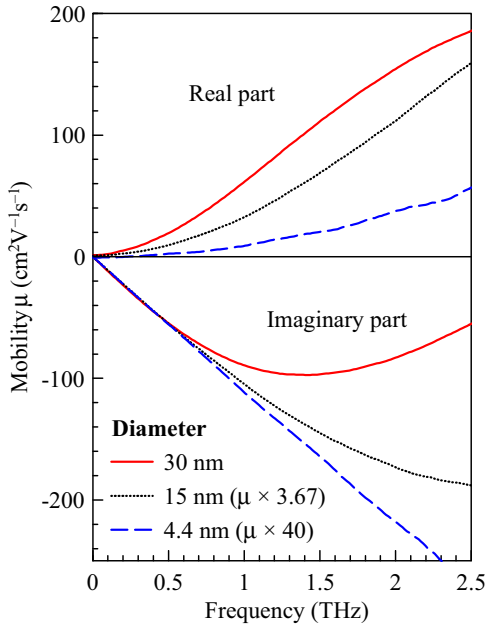

FIG. 3. (Color online) Examples of the mobility spectra of Si NCs with variable size calculated using the Monte Carlo approach. In order to emphasize the difference in the shape of the real part, the spectra are normalized to the same initial slope of the imaginary part (the spectra for 4.4 nm and 15 nm NCs are multiplied by factors 40 and 3.67, respectively).

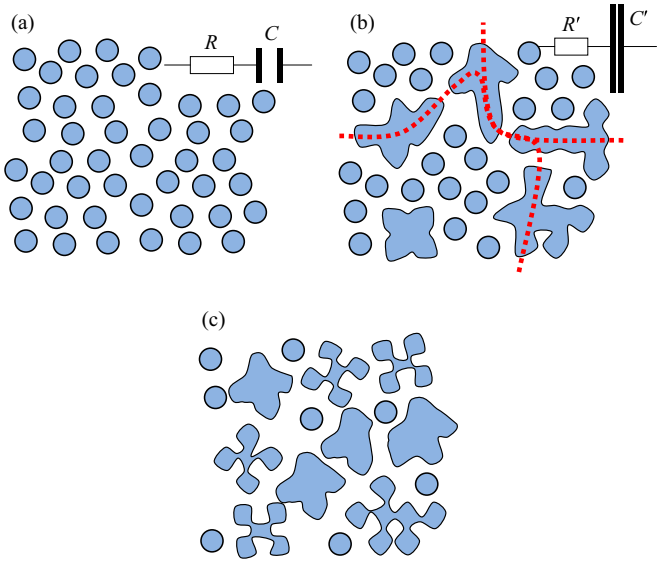

FIG. 4. (Color online) Scheme of the morphology of investigated samples as deduced from THz photoconductivity measurements. (a) NCs in samples S93, M93, M85, and M100 are well isolated from each other and no tendency to aggregation is observed. (b) NCs in the sample M64 start to form clusters; some of these clusters may form a percolation network on a medium length scale (the pathways closest to the percolation are illustrated by thick dotted lines). (c) In thick layers (L93), weakly connected NCs may develop in SiO_x layers at the end of the phase-separation technological step. The electron transport among these NCs is limited. Insets: Equivalent electrical circuits of the structures.

The spectra of sample L93 are qualitatively comparable to those of sample M64, i.e., we can also infer on the presence of clusters. In the fits, we find that almost 30% of Si is present in the form of clusters; this tendency to clustering in thick SiO_x layers is also supported by EF-TEM images [33]. Furthermore, the low-frequency conductivity now slightly deviates from zero, which indicates nonzero (p_F = 5%) probability of inter-NC charge transport (Table I). This shows that the individual NCs are no longer perfectly isolated from each other, but they form at least pairs separated by energy barriers (similar behavior was observed in CdS NCs prepared by chemical bath deposition in [9]). The formation of NCs with nonperfect electrical connection then probably occurs at the end of the phase-separation process when larger-diameter NCs crystallized in thicker SiO_x layers start to touch each other. These aggregates show a worse conductivity than the clusters which form during the initial phase of the NC growth, as pointed out above.

The microscopic picture of the charge-carrier transport in the systems studied is schematically summarized in Fig. 4. We stress that the polarization of the THz pulse is parallel with the sample surface, which means that only the in-plane conductivity is probed. The conclusions on the size of clusters and on the percolation strength thus apply only to lateral directions, whereas information about possible coupling among individual SiO_x layers is not encoded in our signal.

VII. CONDUCTIVITY DYNAMICS

Spectrally unresolved photoconductivity measurements in Fig. 5 show the evolution of the photoconductivity dynamics in the early stages after excitation. On the time scales longer than a few picoseconds, the decay can be described by a single stretched exponential. This is in agreement with the recent report on photoinitiated dynamics of identical samples studied by time-resolved absorption and luminescence [36] where the dynamics was attributed to the nonradiative bimolecular recombination of carriers in the core of Si NCs.

A notable behavior of most of the samples is the presence of a subpicosecond decay component. This feature is particularly pronounced in samples S93 and L93. There is no pronounced excitation fluence dependence of this component (with the exception of sample S93 where the amplitude decreases with increasing excitation fluence). The decay thus cannot be due to Auger recombination, which is a strongly intensity-dependent process. Since NCs were found to be mostly isolated from each other, charge migration towards energetically favorable isolated particles as observed in [18] should not play an important role here; besides that, the subpicosecond time scale is too short for such a process to take place. A fast initial decay component in Si NCs prepared by electrochemical etching was recently attributed to the carrier trapping at interface states [37]. Also one cannot exclude the possibility that the charges are initially generated at higher energy levels in which they are more delocalized; subsequent fast relaxation to more localized states then could manifest itself as a rapid initial drop in the photoconductivity, similarly as it has been observed in CdS NCs [9].

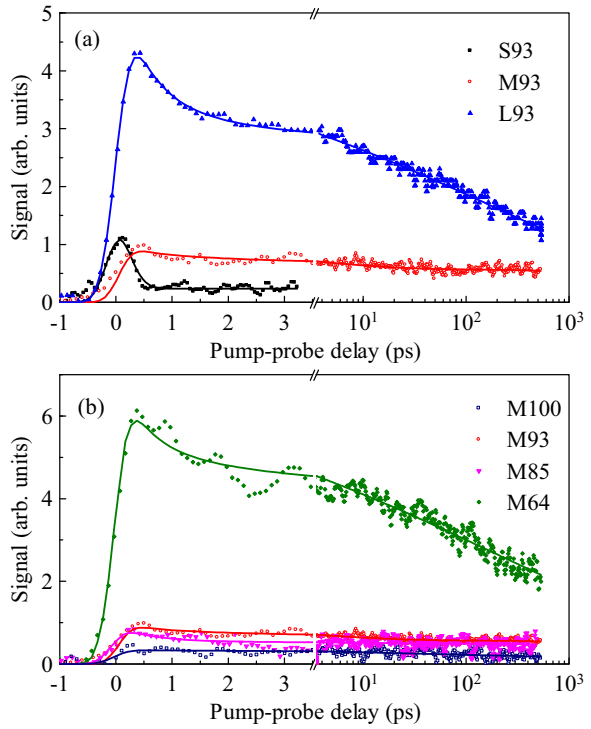

FIG. 5. (Color online) Dynamics of transient conductivity spectra for samples (a) with different SiO_x layer thickness and (b) with different composition x. The pump fluence in all measurements was in the range $3.1-3.6 \times 10^{13}$ photons/cm^2. The lines serve as guides to the eye.

VIII. CONCLUSIONS

Ultrafast photoconductivity of silicon nanocrystals prepared by thermal decomposition of thin nonstochiometric SiO_x layers was investigated by time-resolved THz spectroscopy. We developed a detailed microscopic model of THz effective conductivity, including the effects of sample inhomogeneity and microscopic response of nanocrystals based on classical calculations, which describes the observed THz response over almost two decades of the excitation fluence.

We found that well-isolated Si nanocrystals are formed in layers with high oxygen content and low thickness. Although effects of discrete quantum levels are *a priori* expected for such nanocrystals, our results show that their photoconductivity can still be successfully modeled on a semiclassical basis.

Higher silicon content leads to a progressive creation of large (tens-nm-sized) Si clusters during the technological phase-separation step. These clusters form a short- or medium-range percolation network and do not possess any significant internal structure, which could hinder the intracluster transport of charges. In addition, groups of weakly mutually connected nanocrystals develop in SiO_x layers with a larger thickness. A limited internanocrystal transport through these connections suggests that these structures may develop at the end of the growth of individual nanocrystals inducing higher concentration of defects at the grain boundaries. The size of the observed clusters (tens of nanometers) is large enough to suppress possible effects of the strong quantum confinement.

ACKNOWLEDGMENTS

We acknowledge the Czech Science Foundation which supports the presented research within the project 13-12386S. The work of V.Z. was supported by Grant No. 539612 of the Grant Agency of the Charles University and by the Specific University Research Grant No. SVV-2013-267306.

APPENDIX

The effective optical absorption coefficient α_{eff} can be determined experimentally from transmission measurements. The measured transmittance of 400 nm excitation pulses is provided in Table I and the reflectance of each sample surface was ~4%. We also checked that taking into account the interferences in the superlattice structure does not significantly change the effective absorption. The absorption coefficient α_{eff} was then evaluated (Table I); it ranges between 1×10^4 and 4×10^4 cm^{-1}. In bulk silicon, the refractive index $n_{\text{Si}} \approx 5$ [38] and the absorption coefficient $\alpha_{\text{Si}} \approx 7 \times 10^4$ cm^{-1} [39] at 400 nm.

We may check to which extent such values of α_{eff} and α_{Si} are compatible. For NCs smaller than 10 nm, an effective medium approach can be safely applied even for the wavelengths as short as 400 nm ($d \ll \lambda$). Since the degree of percolation of NCs in our samples is very small, we can use the Maxwell-Garnett model for the effective medium evaluation also at optical frequencies; i.e., we use Eq. (10) from [29] with the following permittivity terms:

$$\varepsilon_p \equiv \varepsilon_{\text{Si}}(400\,\text{nm}) = \left(n_{\text{si}} + i\frac{\lambda}{2\pi}\alpha_{\text{Si}}\right)^2,$$

$$\varepsilon_m \equiv \varepsilon_{\text{SiO2}}(400\,\text{nm}) = 2.15,$$

$$\varepsilon \equiv \varepsilon_{\text{eff}}(400\,\text{nm}) = \left(n + i\frac{\lambda}{2\pi}\alpha_{\text{eff}}\right)^2,$$

where the effective optical refractive index n of the composite layer is unknown. This approach allows us to scan the possible values of absorption in Si NCs (α_{Si}) and calculate the corresponding expected values of α_{eff}. The results are shown in Fig. 6(a) and clearly indicate that α_{eff} is not monotonic and

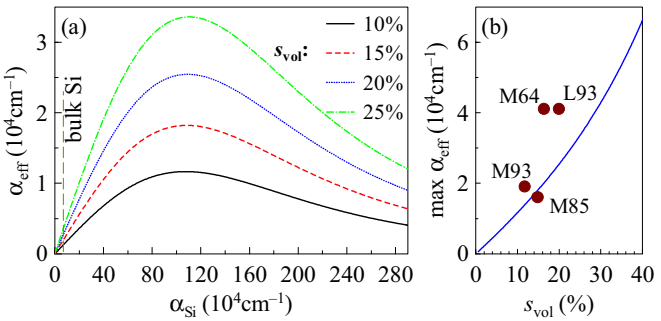

FIG. 6. (Color online) (a) Effective absorption coefficient α_{eff} of a layer with NCs as a function of the absorption coefficient of the NCs α_{Si}. The vertical dashed line denotes the absorption coefficient of bulk Si. (b) Maximum achievable effective absorption coefficient as a function of the volume fraction occupied by the NCs. The symbols indicate the measured absorption coefficient of the investigated samples. Parameters of the calculation are provided in the Appendix.

presents a maximum; regardless of the absorption strength of the Si NCs, α_{eff} then cannot exceed a certain limit value. In our samples, in particular, the measured α_{eff} approaches or even exceeds the upper limit preset by the effective medium model with the given volumic filling fraction of Si NCs determined from EF-TEM experiments. Moreover, this upper limit would be reached only for a very high absorption in the NCs (around 10^6 cm^{-1}).

This discrepancy can be explained if we consider that the blue excitation light is not absorbed only by the Si NCs, but also by other species such as amorphous silicon, compounds with residual nitrogen, or at surface states, which are inevitably present in the samples. These absorption processes contribute to α_{eff} but do not contribute to α_{Si} and do not provide mobile electrons participating in the photoconductivity. The existence of such parasitic absorption excludes the possibility of estimating α_{Si} from transmission measurements. In order to proceed with the analysis, we assume that α_{Si} is equal to the absorption of bulk silicon (7×10^4 cm^{-1}) and describes only the generation of carriers participating in the conductivity. Under such assumption, the product $\phi\alpha_{\text{Si}}$ possesses really the meaning of the concentration of mobile carriers inside Si NCs and, in turn, the quantum yield ξ of carriers participating in the conduction must be formally set to 1. Note that the quantum yield in the formulas for the normalized transient transmission (6)–(8) always appears in the form of the product with the absorption α_{Si} of NCs: these two parameters thus describe the same physics.

[1] L. Pavesi, and R. Turan, *Silicon Nanocrystals. Fundamentals, Synthesis and Applications* (Wiley-VCH, Wienheim, 2010).

[2] L. Khriachtchev, *Silicon Nanophotonics. Basic Principles, Present Status and Perspectives* (Pan Stanford and World Scientific, Singapore, 2009).

[3] N. Koshida, *Device Applications of Silicon Nanocrystals and Nanostructures* (Springer Science+Business Media, New York, 2009).

[4] L. P. Kouwenhoven, C. M. Marcus, P. L. Mceuen, S. Tarucha, R. M. Westervelt, and N. S. Wingreen, *Electron Transport in Quantum Dots, in Mesoscopic Electron Transport, NATO ASI Series* Vol. 345 (Springer, Netherlands, 1997).

[5] K. Storm, F. Halvardsson, M. Heurlin, D. Lindgren, A. Gustafsson, P. M. Wu, B. Monemar, and L. Samuelson, Nat. Nanotech. **7**, 718 (2012).

[6] R. Ulbricht, E. Hendry, J. Shan, T. F. Heinz, and M. Bonn, Rev. Mod. Phys. **83**, 543 (2011).

[7] D. G. Cooke, A. N. MacDonald, A. Hryciw, J. Wang, Q. Li, A. Meldrum, and F. A. Hegmann, Phys. Rev. B **73**, 193311 (2006).

[8] C. S. Ponseca, Jr., H. Němec, J. Wallentin, N. Anttu, J. P. Beech, A. Iqbal, M. Borgström, M.-E. Pistol, L. Samuelson, and A. Yartsev, Phys. Rev. B **90**, 085405 (2014).

[9] Z. Mics, H. Němec, I. Rychetský, P. Kužel, P. Formánek, P. Malý, and P. Němec, Phys. Rev. B **83**, 155326 (2011).

[10] H.-K. Nienhuys and V. Sundström, Appl. Phys. Lett. **87**, 012101 (2005).

[11] P. Parkinson, H. J. Joyce, Q. Gao, H. H. Tan, X. Zhang, J. Zou, C. Jagadish, L. M. Herz, and M. B. Johnston, Nano Lett. **9**, 3349 (2009).

[12] P. Parkinson, C. Dodson, H. J. Joyce, K. A. Bertness, N. A. Sanford, L. M. Herz, and M. B. Johnston, Nano Lett. **12**, 4600 (2012).

[13] H. J. Joyce, C. J. Docherty, Q. Gao, H. H. Tan, C. Jagadish, J. Lloyd-Hughes, L. M. Herz, and M. B. Johnston, Nanotechnology **24**, 214006 (2013).

[14] H. Němec, V. Zajac, I. Rychetský, D. Fattakhova-Rohlfing, B. Mandlmeier, T. Bein, Z. Mics, and P. Kužel, IEEE Trans. Terahertz Sci. Technol. **3**, 302 (2013).

[15] V. Zajac, H. Němec, C. Kadlec, K. Kůsová, I. Pelant, and P. Kužel, New J. Phys. **16**, 093013 (2014).

[16] D. G. Cooke, A. N. MacDonald, A. Hryciw, A. Meldrum, J. Wang, Q. Li, and F. A. Hegmann, J. Mater. Sci.: Mater. Electron **18**, S447 (2007).

[17] N. V. Smith, Phys. Rev. B **64**, 155106 (2001).

[18] D. G. Cooke, A. Meldrum, and P. Uhd Jepsen, Appl. Phys. Lett. **101**, 211107 (2012).

[19] L. V. Titova, T. L. Cocker, D. G. Cooke, X. Wang, A. Meldrum, and F. A. Hegmann, Phys. Rev. B **83**, 085403 (2011).

[20] E. Hendry, M. Koeberg, B. O'Regan, and M. Bonn, Nano Lett. **6**, 755 (2006).

[21] P. Kužel, and H. Němec, J. Phys. D: Appl. Phys. **47**, 374005 (2014).

[22] M. Zacharias, J. Heitmann, R. Scholz, U. Kahler, M. Schmidt, and J. Bläsing, Appl. Phys. Lett. **80**, 661 (2002).

[23] M. Jivanescu, D. Hiller, M. Zacharias, and A. Stesmans, Europhys. Lett. **96**, 27003 (2011).

[24] A. M. Hartel, D. Hiller, S. Gutsch, P. Löper, S. Estradé, F. Peiró, B. Garrido, and M. Zacharias, Thin Solid Films **520**, 121 (2011).

[25] L. Fekete, P. Kužel, H. Němec, F. Kadlec, A. Dejneka, J. Stuchlík, and A. Fejfar, Phys. Rev. B **79**, 115306 (2009).

[26] S. Gutsch, J. Laube, A. M. Hartel, D. Hiller, N. Zakharov, P. Werner, and M. Zacharias, J. Appl. Phys. **113**, 133703 (2013).

[27] J. López-Vidrier, Y. Berencén, S. Hernández, O. Blázquez, S. Gutsch, J. Laube, D. Hiller, P. Löper, M. Schnabel, S. Janz, M. Zacharias, and B. Garrido, J. Appl. Phys. **114**, 163701 (2013).

[28] T.-I. Jeon and D. Grischkowsky, Phys. Rev. Lett. **78**, 1106 (1997).

[29] H. Němec, P. Kužel, and V. Sundström, J. Photochem. Photobiol. A **215**, 123 (2010).

[30] H. Němec, P. Kužel, and V. Sundström, Phys. Rev. B **79**, 115309 (2009).

[31] F. Wang, J. Shan, M. A. Islam, I. P. Herman, M. Bonn, and T. F. Heinz, Nat. Mater. **5**, 861 (2006).

[32] P. Hapala, K. Kůsová, I. Pelant, and P. Jelínek, Phys. Rev. B **87**, 195420 (2013).

[33] S. Gutsch, Ph.D. thesis (Albert-Ludwigs-Universität, Freiburg im Breisgau, 2014).

[34] S. Gutsch, D. Hiller, J. Laube, M. Zacharias, and C. Kübel, Beilstein J. Nanotechnol. **6**, 964 (2015).
[35] G. L. Dakovski, B. Kubera, S. Lan, and J. Shan, J. Opt. Soc. Am. B **23**, 139 (2006).
[36] M. Kořínek, M. Kozák, F. Trojánek, D. Hiller, A. Hartel, S. Gutsch, M. Zacharias, and P. Malý, Physica E **56**, 177 (2014).
[37] K. Žídek, F. Trojánek, P. Malý, L. Ondič, I. Pelant, K. Dohnalová, L. Šiller, R. Little, and B. R. Horrocks, Opt. Express **18**, 25241 (2010).
[38] H. R. Philipp and E. A. Taft, Phys. Rev. **120**, 37 (1960).
[39] J. Noffsinger, E. Kioupakis, C. G. Van De Walle, S. G. Louie, and M. L. Cohen, Phys. Rev. Lett. **108**, 167402 (2012).